

Low Frequency Modes in Heme Proteins

Florin Rosca, Anand T. N. Kumar, Dan Ionascu, Xiong Ye, Andrey A. Demidov, and Paul M. Champion*

Physics Department and Center for Interdisciplinary Research on Complex Systems, Northeastern University, Boston, MA 02115, USA

(Received October 29, 2001)

The technique of femtosecond coherence spectroscopy is applied to heme protein samples. Strong oscillations are detected near 40 cm^{-1} in all of the samples studied. Additional modes near 80, 120, and 160 cm^{-1} are observed in the photochemically active samples. A simple harmonic model is not able to account for the observed relative intensities of these modes or the carrier wavelength dependence of their frequency and phase. As a result, we develop an anharmonic model where the oscillatory signal is damped as the result of heterogeneity in the potential surface. The source of the heterogeneity in the anharmonic potential surface is correlated with the inhomogeneous broadening of the Soret band. The higher harmonics in the photochemically active samples demonstrates that the anharmonic mode is strongly coupled to the ligand photodissociation reaction (i.e., upon photolysis it is displaced far from equilibrium). Moreover, the observation of the ~40 cm^{-1} oscillations in all of the iron based heme protein samples, including porphine and protoporphyrin IX model compounds, suggests that this mode is associated with nuclear motion of the core of the porphyrin macrocycle. As a result, we suggest that the reaction coupled oscillations at ~40 cm^{-1} and ~80 cm^{-1} are a direct reflection of anharmonic heme doming dynamics.

Femtosecond coherence spectroscopy (FCS) is a pump–probe technique that utilizes the spectral bandwidth associated with ultrafast laser pulses to prepare and monitor coherent states in resonant and nonresonant samples.[1–12] This technique allows the real time observation of ultrafast processes, so that the frequencies and the initial phases of the detected vibrational oscillations can be measured and compared. Following the pump pulse excitation, two types of processes can occur that we refer to as "field driven" and "reaction driven". In the first case the pump pulse excites the Raman active modes of the sample without affecting its structure. In the "reaction driven" case, the photoexcited state rapidly decays, via non-radiative channels, into a coherent "product state". In both cases, the delayed probe pulse monitors the pump induced transient absorption changes in the sample. The relaxation dynamics of the non-equilibrium structure generated by the ligand photodissociation reaction in heme proteins has been extensively studied over a wide range of timescales using a variety of techniques.[13–24]

Ligand photolysis excites low frequency heme/protein oscillations that arise from the forces associated with electronic rearrangements in the iron d-orbitals that take place when the iron atom undergoes a spin transition upon ligand dissociation.[6,12] These low frequency modes are also potentially connected to energy transport and signal transduction between the active site and the protein backbone and can thus affect the physiological functionality of the protein. One particular vibrational degree of freedom that we have suggested[25–27] is highly relevant to the ligand binding and dissociation reaction is heme "doming", which corresponds to heme motion that changes the local equilibrium position of the iron atom. The iron atom changes from an in-plane position, when the diatomic ligand is bound, to an out-of-plane (~0.4Å) position[28] in the unligated state, which is distributed and dependent on the surrounding protein conformation.[25–27] Normal mode calculations[29–31] and analysis of the non-exponential ligand rebinding[23] in Mb predict[25–27] that heme doming oscillations in the unligated state should be near 50 cm^{-1}.

In this work we present data displaying a strong vibrational mode near 40 cm^{-1}, denoted as ν_{40}, as well as an additional sample dependent vibrational mode near 80 cm^{-1}, which we denote as ν_{80}. The observation of ν_{40} in deoxy Mb, and ν_{40} and ν_{80} in MbNO was reported earlier.[6,32] Here, we study the amplitude and phase behavior of ν_{40} and ν_{80} in MbNO as the pump/probe carrier wavelength is tuned across the Soret absorption band. A heterogeneous anharmonic potential model is used to simulate the oscillatory signals that give rise to ν_{40} and ν_{80} (and sometimes higher harmonics) in the power spectra of the photolyzed samples. These signals are assigned to motions associated with anharmonic heme doming dynamics.

Materials and Methods

The pump–probe setup and the preparation of the heme protein samples has been described in detail elsewhere.[32,33] In order to both pump and probe the studied samples, we tune the laser carrier frequency into resonance with the strong Soret absorption band in the 400–450 nm region. This allows us to selectively probe the dynamics of the active site (heme) and its interaction with the protein. For all experiments presented in this paper we use the open band detection scheme in which the full spectrum of the probe beam is detected by a photodiode. This detection scheme facilitates accurate phase measurements for the oscillatory signal be-

cause the autocorrelation measurement that defines the pump–probe zero time delay also uses the open band detection.

The concentration of protein is chosen so that the sample has an absorbance of about 0.6 OD at the pump wavelength in a 0.5 mm cell. Each data set is the average of 60–120 scans of the optical delay line, generated in a 2–4 h experiment. In order to ensure sample integrity, the absorption spectrum of the sample is measured before and after each experiment and intermediate FCS files are routinely compared in order to gauge the sample stability during the course of the experiment.

Typical measured signals for resonant samples consist of damped oscillations superimposed on a monotonically decaying background. The coherence coupling signal that dominates the signal around the zero time delay is truncated before data analysis. To generate the power spectrum associated with the time resolved oscillatory signal we use a linear predictive singular value decomposition (LPSVD) algorithm[34], which simultaneously fits both the oscillations and the monotonic decay. This algorithm extracts the oscillatory parameters such as frequency, phase, amplitude and damping factors, as well as the exponential parameters of the (zero frequency) monotonic background. An alternative method of analysis involves preliminary fitting of the monotonic background using the maximum entropy method (MEM), which uses a distribution of exponential decay rate constants.[35] The residual oscillatory signal is subsequently fit using LPSVD or a Fourier transform algorithm. The fits are considered stable when both techniques generate the same power spectrum for the oscillatory signals.

Results

A. Photostable Samples. Since we try to enhance the low frequency part of the vibrational spectrum, we use the longest pulses (80–100 fs) (corresponding to the narrowest bandwidth) generated by the laser. The open band detection, in contrast to the highly detuned detection used in earlier studies[6], also enhances the low frequency modes.[32,36] When probing deoxy Mb, which is photostable, the coherent oscillations are induced by the forces developed during the pump pulse, which arise from the differences between the ground and resonant excited electronic state potential energy surfaces. Since for heme proteins the resonant π–π^* Soret excited state is very short lived and the population decay takes place within 10–100 fs[37–41], we assign the long–lived (~1–2 ps) oscillatory signals to the ground electronic state. This assignment is verified by white light continuum measurements of the transient absorption spectrum in the Soret region.[42]

The presence of a ~40 cm^{-1} mode can be clearly seen in the oscillatory signal of deoxy Mb and in the LPSVD generated power spectrum presented in the first panel of Fig. 1. The presence of a ~40 cm^{-1} oscillation in porphine substituted Mb (third panel of Fig. 1) and in the FePPIX model compound (second panel) suggests that the source of the ν_{40} oscillation is associated with the core of the porphyrin macrocycle and does not depend strongly on the peripheral substituents or the sur-

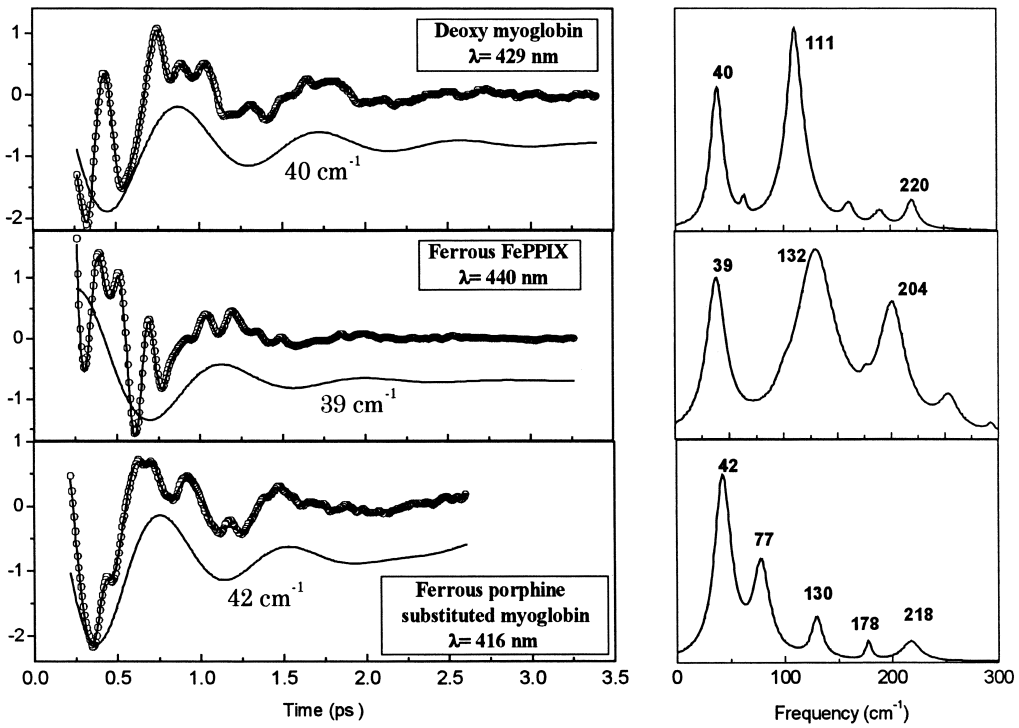

Fig. 1. Sequence of experiments using the open band detection scheme on three different heme proteins. The left panels present the oscillatory part of the generated signal, and the right panels show the corresponding power spectra. The ~40 cm^{-1} oscillation used in the fit is shown displaced from the data as a solid line. The exponential damping factors for the ~40 cm^{-1} oscillation are 0.5 ps for the model systems in the lower two panels and 0.7 ps for deoxy Mb. The sample and the pump/probe carrier wavelength are given in the right upper corner of the left panels.

rounding protein. Another possible source of ν_{40}, such as the torsional motion of histidine 93, is inconsistent with the presence of modes at 43 cm^{-1} and 39 cm^{-1} in other heme samples that do not have a histidine ligand (not shown).

B. Photochemically Active Samples. In section A, we have focused on non-reactive compounds, where the vibrational coherences are driven by the electric field interventions of the ultrafast pump laser pulse. Another important characteristic of time resolved FCS is its ability to monitor chemical reactions and the subsequent evolution of the non-equilibrium product state. In this section, we present FCS experiments on several photochemically active samples. The experimental data for some of these samples are plotted, along with the LPSVD fits and power spectra, in Figs. 2 and 3. The most distinguishing feature of the results in Figs. 2 and 3, compared to the non-reactive samples, is the presence of a second mode at ~80 cm^{-1} (and sometimes higher harmonics at ~120 cm^{-1} and ~160 cm^{-1}), in addition to the low frequency mode near 40 cm^{-1}. The mode near 80 cm^{-1} is significantly enhanced relative to ν_{40} when detuned detection conditions are employed[32,36,43] and, as a result, ν_{80} was emphasized in earlier studies[6] conducted under detuned conditions.

Both ν_{40} and ν_{80} show slight sample dependent variations in frequency, but the higher frequency mode remains approxi-

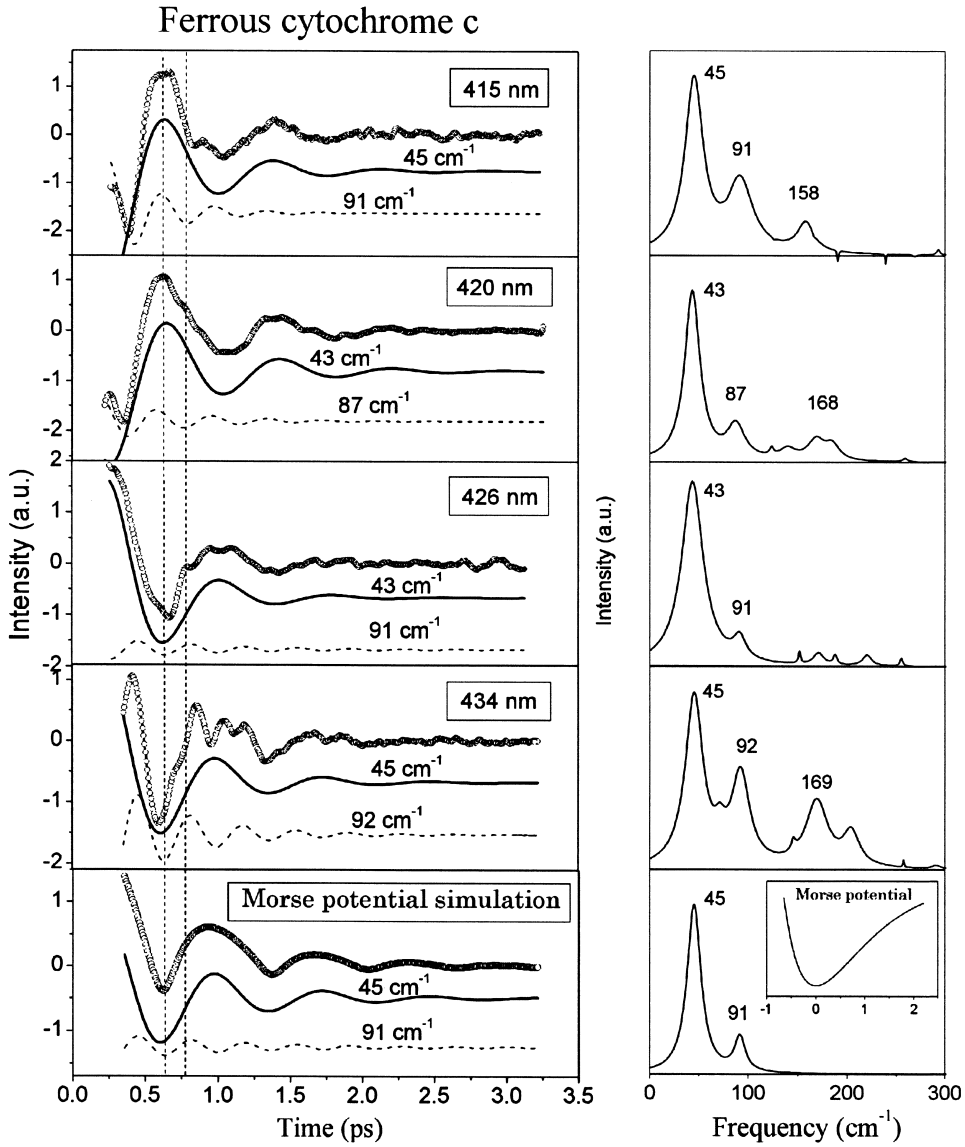

Fig. 2. Sequence of experiments using the open band detection scheme on ferrous cytochrome c for four pump/probe carrier wavelengths. The left panels present the oscillatory part of the signal, and the right panels show the corresponding power spectra. The ~44 cm^{-1} oscillation (solid line) and the ~89 cm^{-1} oscillation (dashed line) used in the fit are shown displaced from the data. The exponential damping factor for these modes is 0.5 ps. One can observe a π phase flip for both modes in the 420–426 nm spectral region. The left lower panel displays the simulated signal generated by the dynamics of a particle in a Morse potential ($U_g(q) = e^{-2q} - 2e^{-q}$), along with the 45 and 91 cm^{-1} oscillations used for its fit. The lower right panel presents the associated power spectrum and a plot of the Morse potential (in the inset).

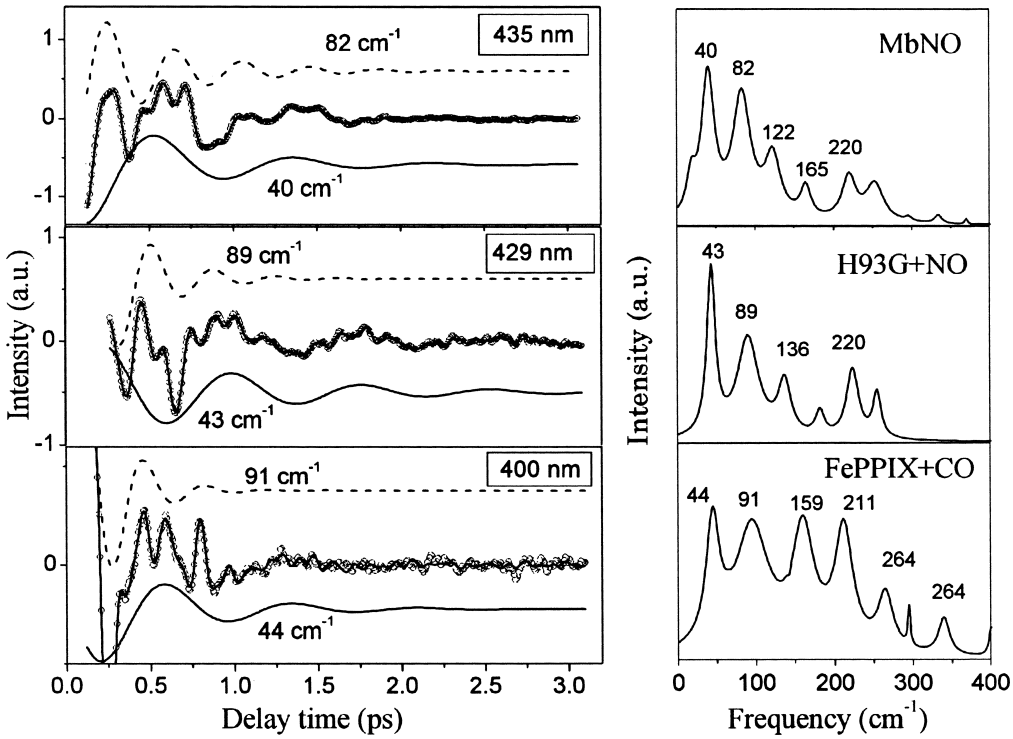

Fig. 3. Sequence of experiments using the open band detection scheme on three photochemically active samples (MbNO, NO bound H93G Mb and CO bound FePPIX+2MeIm). The left panels display the oscillatory part of the generated signal, and the right panels show the corresponding power spectra. The ~40 cm^{-1} oscillation (solid line) and the ~80 cm^{-1} oscillation (dashed line) used in the fit are shown displaced from the data. The relative damping of ν_{40} and ν_{80} can be compared by using the line widths of the power spectrum. The values for γ_{40} and γ_{80} are 0.57 ps and 0.49 ps (MbNO), 0.8 ps and 0.33 ps (H93G+NO), and 0.5 ps and 0.2 ps (FePPIX+CO).

mately twice the frequency of the low frequency mode. The frequency pairs observed are 41–81 cm^{-1} in MbNO, 46–91 cm^{-1} in HbNO, 44–89 cm^{-1} in ferrous cytochrome c, 43–87 cm^{-1} in NO bound H93G Mb and 44–91 cm^{-1} in CO bound FePPIX. The fact that the higher frequency oscillations near 80 cm^{-1} are approximately twice the frequency of the oscillations near 40 cm^{-1} is suggestive of a harmonic sequence. In the case of MbNO, even higher harmonics appear to be present at 122 cm^{-1} and 165 cm^{-1} (see top panel of Fig. 3 and previous reports[12,32]).

Furthermore, the low frequency oscillations seen in the MbNO sample near 40 cm^{-1} exhibit a continuous drift from 40 cm^{-1} to 46 cm^{-1}, as the laser carrier wavelength is tuned towards the red (450–470 nm) of the product state (deoxy Mb) Soret absorption band. This frequency drift follows the same general pattern observed for the field driven coherence in deoxy Mb. However, the frequency of the oscillations near 80 cm^{-1} always remains nearly twice the frequency of ν_{40}. These observations strongly suggest that ν_{80} forms part of a harmonic progression with ν_{40} as the fundamental frequency.

Another example of photochemical activity is ferrous cytochrome c, which was recently shown[44] to undergo a rapid ligand (methionine) photodissociation reaction followed by ~6 ps geminate rebinding. The oscillatory part of the FCS signal of ferrous cytochrome c is presented at four different carrier wavelengths in the first four panels of Fig. 2, along with the corresponding LPSVD power spectra. The main features observed in the signal are a damped ~44 cm^{-1} oscillation (ν_{40}) and a ~89 cm^{-1} oscillation (ν_{80}) of smaller amplitude. Both of these modes exhibit a π phase flip and a dip in amplitude around 423 nm, which is close to the product state transient absorption maximum (found near 425 nm from white light continuum experiments[44]). The amplitude of ν_{80} seems to decrease faster than ν_{40} as the laser pulse carrier wavelength approaches 423 nm. The data generated at 423 nm are not shown because of the lack of an oscillatory signal. The ~44 cm^{-1} and ~89 cm^{-1} oscillations used in the LPSVD fit to the data are depicted as solid and dashed lines, respectively (shifted from the data for clarity). The two vertical lines going through all panels are helpful in comparing the relative phases of the oscillatory components. An important observation is the coincidence of the ~89 cm^{-1} oscillation maxima or minima with the maxima and minima of the ~44 cm^{-1} oscillation and the fixed relative phase at all carrier wavelengths.

The oscillatory parts of the open band FCS signals in three different photochemically active samples (MbNO, NO bound H93G Mb and CO bound FePPIX+2MeIm) are displayed in Fig. 3, along with the corresponding power spectra. The CO bound FePPIX model complex was studied using a lower repetition rate amplified laser system[33] so that sample reset would be assured between the arrival of the pump-probe pulse pairs. The ν_{40} and ν_{80} oscillations used in fitting the data are depicted as solid and dashed lines (shifted for clarity). The Fe–His mode characteristic of deoxy Mb is found near 220 cm^{-1} in the

power spectrum when the protein material is present and is downshifted to 211 cm^{-1} for the FePPIX model complex.[45] The low frequency modes present in the power spectra of MbNO (upper right panel in Fig. 3) seem to form a four-term harmonic sequence (41, 82, 123, 164 cm^{-1}). This harmonic sequence is present in numerous data sets generated using MbNO.[12,32] The weaker shoulder near 20 cm^{-1} has been the subject of independent experiments.[46,47]

Discussion

The technique of FCS is very useful for monitoring the nuclear motions associated with biomolecular reaction dynamics, especially in the low frequency region of the vibrational spectrum. We have documented the presence of a mode near 40 cm^{-1} (ν_{40}) in the photostable heme proteins. In addition, we have found that the photochemically active heme samples display a harmonic progression involving this mode. The frequency, phase, and amplitude dependence of ν_{40} and ν_{80} have been studied for deoxy Mb, MbNO and ferrous cytochrome c as a function of the pump/probe carrier wavelength.

A. Phase and Frequency of ν_{40}. For deoxy Mb we observe a discrepancy between the phase behavior of ν_{40} and the theoretical prediction[43] based on a simple linear harmonic model. In contrast, the simple linear harmonic model (with inhomogeneous broadening) provides an excellent description of the phase behavior of the Fe–His mode at 220 cm^{-1}. One possible source for the discrepancy for ν_{40} might have to do with the fact that the transient absorption lineshape of photoexcited deoxy Mb evolves on the same timescale as the ν_{40} oscillation ($T_{40} \sim$800 fs).

The drift of the frequency of ν_{40} as the carrier wavelength is tuned across the Soret absorption band is probably linked to the inhomogeneities and structural disorder of the heme system in deoxy Mb. As discussed earlier, the deoxy Mb absorption spectrum shows strong evidence of inhomogeneous broadening[26,27,48] and the highly asymmetric inhomogeneous lineshape of Mb has been ascribed to disorder in the equilibrium position of the central iron atom that is correlated with the ligand binding kinetics.[26,27,48] This is of relevance to the low frequency oscillations localized at the heme, which may involve the doming motion of the iron atom. Apart from a simple distribution in the equilibrium position of the heme iron[27], the experimental data suggest that the vibrational frequency of ν_{40} is also distributed.

A major topic addressed in this paper concerns the assignment of ν_{40} and ν_{80} and the question of whether these modes are part of a harmonic progression or are independent fundamentals. In early work[6], which utilized detuned detection, we assigned ν_{80} as the doming mode. This assignment was based upon the fact that although ν_{40} appeared in the power spectrum[6], it was essentially undetectable in the raw data. However, recent advances in detection technique[32,47] have made the existence of ν_{40} unequivocal and have revealed modes at even lower frequencies.[46] An important observation, which strongly indicates that ν_{80} is a harmonic of ν_{40}, is the fact that $\nu_{80} \approx 2\nu_{40}$ under a variety of conditions (e.g., as carrier wavelength is varied, or as the sample is changed). These results suggest that these two modes are not independent vibrational fundamentals and force us to look for theoretical models that are consistent with those observations.

B. Harmonic Model. In considering the possibility that the low frequency progressions in Figs. 2 and 3 constitute an overtone or harmonic sequence, one can eliminate a simple linearly displaced harmonic oscillator model. Calculations[43] based on the linearly displaced harmonic model, where the main source of overtone intensity comes from the "double pass" of the wavepacket across the probe detection region, predict that the intensities of the overtones are generally much smaller than the fundamental signals, as seen in the upper left panel of Fig. 4. The double pass contribution can be understood through the time dependent first moment of the vibrational coordinate that modulates the centroid of the equilibrium absorption spectrum. For example, consider a single mode coupled to a two electronic level system, with frequency ω_0 and electron-nuclear coupling force $f = \Delta(m\omega_0^3\hbar)^{1/2}$ (where Δ is the dimensionless displacement between the ground and excited state). The pump interaction drives the nuclei out of equilibrium. If we let the time-dependent mean nuclear position after the pump interaction be $\langle Q(t)\rangle$, the correlation function that describes the response of the pump-induced non-stationary system can be shown to be of the form[43]

$$C_{\mathrm{neq}}(t,t') = K(t-t') \exp\left[\left(\frac{if}{\hbar}\right)\int_{t'}^{t} ds\langle Q(s)\rangle\right], \quad (1)$$

where $K(t-t')$ is an equilibrium correlation function (also called the optical absorption correlator) that describes the equilibrium lineshape of the system. For a harmonic potential, the mean position $\langle Q(t)\rangle$ oscillates only at the fundamental frequency. In this case, the centroid of the non-equilibrium lineshape induced by the pump pulse oscillates about the equilibrium absorption maximum at the fundamental oscillator frequency. It is then clear that the amplitude of the fundamental signal is proportional to the derivative of the absorption lineshape, so that the oscillatory amplitude is largest near the shoulders of the absorption spectrum, but vanishes at band center. On the other hand, the overtone amplitude profile is related to the second derivative of the absorption spectrum and naturally exhibits a contrasting behavior from the fundamental. (Here we ignore the very small contributions from the higher moment, i.e., $\langle Q^2(t)\rangle$ "squeezed" modulations, of the pump induced vibrational wavepacket.[49]) As seen in the upper left panel of Fig. 4, the overtones are peaked at the resonant absorption maximum, where the wavepacket passes twice per period of oscillation, and exhibit an amplitude dip at two points near the shoulders of the absorption spectrum. Within this simple homogeneous harmonic model[43], the fundamental and overtone phase profiles exhibit a π phase change associated with every dip in amplitude, generating the different phase behavior displayed in the upper right panel of Fig. 4. This behavior is clearly not observed for ν_{40} and ν_{80} in the experimental results reported here (e.g., see Fig. 2), where the two modes have nearly equivalent intensities and display similar phase and amplitude profiles.

C. Anharmonic Models. On the other hand, if we consider an asymmetric anharmonic potential for the low frequency mode, we can explain many of the features observed in the experimental data. The assumption that the motion associated with ν_{40} takes place in an asymmetric anharmonic potential is

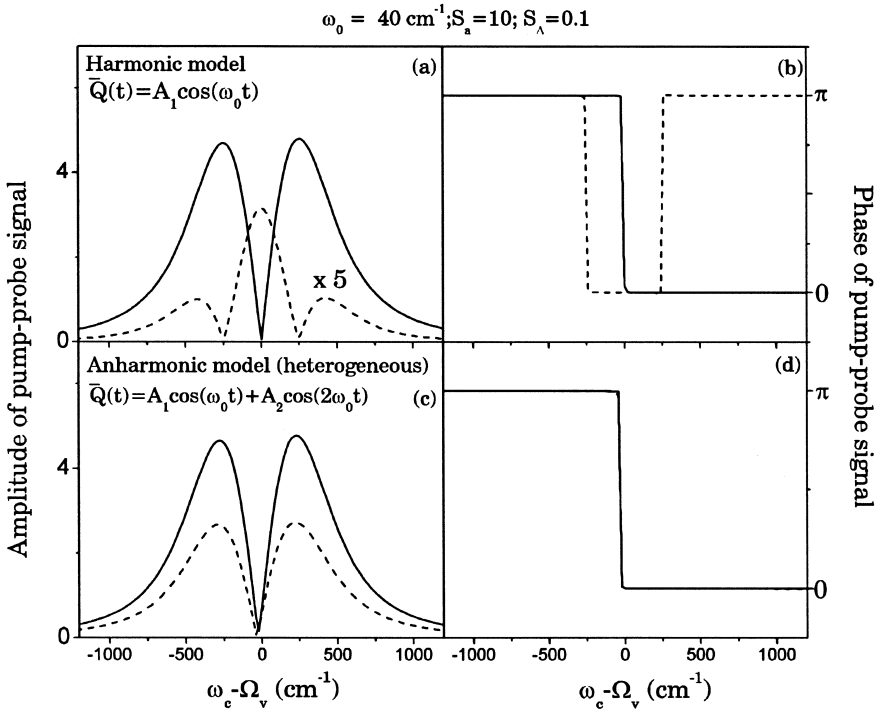

Fig. 4. Comparison of the open band amplitude and phase profiles for a harmonic and anharmonic oscillator model. Panels (a–b) show the open band amplitude and phase profiles for the fundamental (solid) and overtone (dashed) signals for a 40 cm^{-1} mode coupled to a two electronic level system. Panels (c–d) show the corresponding profiles for an anharmonic model that approximates the mean position of the oscillator $Q(t)$ to be adequately described by the first two harmonics of the Fourier series, with amplitudes A_1 (solid) and A_2 (dashed). For both the simulations, the non-stationary state was assumed to be a thermal state displaced from equilibrium.

quite reasonable, considering that the iron atom is coordinated only to the histidine on the proximal side, following the pump induced ligand photodissociation reaction. As an example, we take the rescaled Morse potential plotted in the inset in the lower right panel of Fig. 2.

In order to simulate the first moment dynamics of the position coordinate associated with vibrational oscillations in an anharmonic potential, we place a particle in the Morse potential with a large initial displacement (which justifies the classical description). We then follow the dynamics induced by the restoring force $F(q)$ and the intrinsic damping. The simulated oscillatory signal for the homogeneous anharmonic model and the corresponding LPSVD power spectrum are presented in the upper panel of Fig. 5. In this case, the only source of signal decay is the inherent damping present in the expression for coordinate motion $(-\gamma_{\text{int}}\dot{Q})$.

For small initial displacements, the Morse potential can be well approximated as a harmonic potential and the dynamics resembles a simple damped harmonic oscillator. However, higher harmonics are needed to fit the simulated dynamics for large displacements. The relative amplitude of these higher harmonics (compared to the fundamental) increases as the initial displacement gets larger and the particle samples more anharmonic regions of the Morse potential. The intrinsic damping tends to decrease the amplitude of the oscillations so that the particle returns to regions of the potential closer to the equilibrium position, associated with higher frequencies. As a result, for large initial displacements, the oscillatory frequency effectively becomes time dependent ($\omega_0 \rightarrow \omega_0(t)$), starting at lower frequencies and evolving towards higher frequencies as the system damps (see simulated signal in the upper panel of Fig. 5). The LPSVD algorithm fits such a signal with a low frequency and short lifetime component (e.g., 36 cm^{-1}) for the early time signal and with a longer-lived higher frequency component (e.g., 49 cm^{-1}) for the signal at later times. This generates the power spectrum presented in the inset of the upper panel of Fig. 5. Since the experimental signals do not display a time-dependent oscillatory frequency (i.e., a single peak in the power spectrum is sufficient to fit the fundamental oscillation), we are led to a different version of the anharmonic model. In this alternative version, the dominant damping mechanisms are due to the *inhomogeneous* nature of the system and pure dephasing, rather than to population decay. The experimentally observed oscillatory signals can be damped by sources other than population decay. For example, the protein conformational substates discussed earlier lead to correlated distributions of heme out-of-plane geometry and doming frequency. The distribution of vibrational frequencies will broaden the spectral line as well as damp the oscillatory signals. We also note that, since the oscillatory frequency in an anharmonic potential depends on the initial displacement, conformational inhomogeneities can induce a distribution of frequencies through either a distribution of initial displacements or through a distribution in the shape (curvature) of the potential (or both). Finally, if the protein and/or solvent undergo structural fluctuations on faster timescales, pure dephasing[50] (bath induced en-

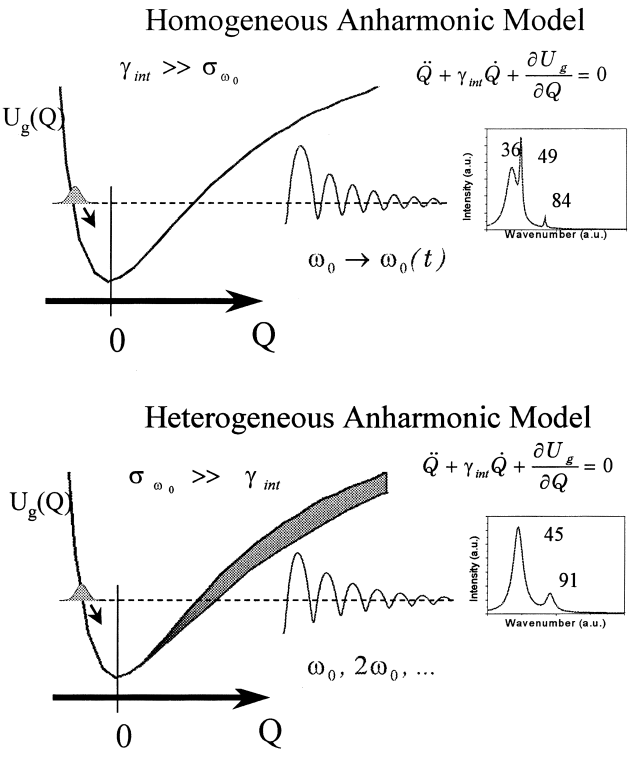

Fig. 5. The signals simulated using the dynamics of a particle initially displaced on a Morse potential ($U_g(q) = e^{-2q} - 2e^{-q}$), as well as the corresponding power spectra, are presented considering two sources of damping. In the upper panel we consider the inherent homogeneous population damping ($\gamma_{int} >> \sigma_{\omega_0}$) which is analogous to "friction" on the potential surface. Due to the decreasing oscillatory amplitude in the anharmonic potential, the simulated signal contains time dependent frequencies, which are fit with LPSVD using two damped cosine functions with different lifetimes. In the lower panel, the damping factor is introduced as an inhomogeneous frequency distribution ($\sigma_{\omega_0} >> \gamma_{int}$), which is associated with pure dephasing and/or different potential curvatures. The signal simulated using the heterogeneous anharmonic model is fit by LPSVD with a damped fundamental oscillation and its higher harmonics.

ergy level fluctuations) will result, which is another form of line broadening without population decay.

As an example, a distribution in the curvature of the potential is presented in the lower panel of Fig. 5. In this heterogeneous anharmonic model, the inhomogeneous broadening (or pure dephasing) is considered to be larger than the intrinsic damping due to population decay ($\sigma_{\omega_0} >> \gamma_{int}$). To generate the simulated signal within this model we allow the system to evolve on the anaharmonic potential with small inherent damping ($-\gamma_{int}\dot{q}$). For the dynamics generated under these conditions, the amplitude of oscillations and, hence, the fundamental oscillatory frequency remains almost constant in time. This means that the coordinate $Q(t)$ can be well described using a Fourier series involving only the fundamental frequency and its higher harmonics i.e., $Q(t) = \Sigma_n Q_n \cos(n\omega_0 t + \phi_n)$. The final simulated signal is then assumed to follow the first moment dynamics and is generated by convolving the dynamics of a single protein molecule over a frequency distribution (due to inhomogeneity or pure dephasing) that is commensurate with the experimentally observed peak width in the power spectrum ($\sim$12 cm^{-1}).

Within this model, we write the signal for a single undamped anharmonic oscillator as a Fourier series:

$$S_h(\omega_0, \omega_c, \tau) = \sum_{n=1}^{\infty} A_n \cos(n\omega_0\tau + \phi_n). \quad (2)$$

Here, the summation is over all the harmonics of the fundamental mode frequency ω_0 and the optical carrier frequency dependence of the final signal is denoted by ω_c. For simplicity, we assume that, for a narrow frequency distribution, the amplitudes A_n of the various overtones do not depend on the mode frequency. If the inhomogeneous vibrational distribution is specified by a mean vibration frequency $\bar{\omega}_0$ and a function $f(\bar{\omega}_0 - \omega_0)$, the final signal is obtained from a simple convolution of the above expression with the inhomogeneous distribution:

$$S_I(\bar{\omega}_0, \omega_c, \tau) = \int d\omega_0 f(\bar{\omega}_0 - \omega_0) S_h(\omega_0, \omega_c, \tau). \quad (3)$$

The observed signal is well described by this model, using a fundamental oscillation and its higher harmonic, as seen in the associated LPSVD power spectrum in the lower panels of Figs. 2 and 5. A Lorentzian distribution for $f(\bar{\omega}_0 - \omega_0)$ was used in these simulations.

If we consider an anharmonic potential for the vibrational coordinate, the first moment modulation $\langle Q(t) \rangle$ in Eq. 1 directly contains the higher harmonics of the fundamental frequency. Consequently, the centroid of the lineshape is modulated at the higher harmonics, as well as at the fundamental frequency. The amplitude and phase profiles of such harmonics, when detected in a pump-probe experiment, are expected to track the amplitude and phase profile of the fundamental, i.e. the amplitudes dip and their phase flips by π at the absorption maximum. This is illustrated in the lower panels of Fig. 4.

The presence of a π phase flip and amplitude dip in ferrous cytochrome c around 423 nm for both ν_{40} and ν_{80} (see Fig. 2) agrees well with the predictions made using the above model. We have used a Gaussian frequency distribution equivalent to a $\sim$12 cm^{-1} inhomogeneous broadening of the 45 cm^{-1} mode to generate the simulated signal presented in the lower panel of Fig. 2. The simulations look very similar to the oscillatory signal measured in ferrous cytochrome c at 426 and 434 nm presented in the third and fourth panels (and to the signal measured at 415 and 420 nm when the π phase shift is added). The similarity is connected to the fixed relative phase relation between ν_{40} and ν_{80} in the experimental and simulated data as seen in Fig. 2. The alignment of the maxima and minima of these oscillatory components is the key condition needed to generate the pattern observed in the experimental data. The good agreement, observed between the experimental data for ferrous cytochrome c and the simulations, makes a strong case for a description of the nuclear coordinate motion using an anharmonic potential surface.

Similar behavior is observed for ν_{40} and ν_{80} in MbNO. The

80 cm^{-1} mode displays a phase flip and a dip in amplitude near 427 nm. The phase of the 40 cm^{-1} mode presents a slower π phase shift in the 427 nm region, which is not associated with a clear dip in amplitude. This observation is anomalous and may signal the presence of more complex electron-nuclear coupling (e.g., quadratic coupling), which can shift the phase and amplitude transition points away from the absorption maximum.[43] The phase drift observed in the 445–480 nm region for both the ν_{40} and the ν_{80} modes in MbNO is probably correlated to the frequency drift displayed in the same spectral region. The carrier wavelength dependence of both the frequency and phase may be related to the underlying inhomogeneity associated with the deoxy Mb Soret band. Thus, the carrier wavelength may resonantly select a subpopulation of conformational states that have different values of ν_{40}. Such a scenario is consistent with the concept of a distribution of anharmonic potential surfaces that is correlated with the distribution of electronic transition energies. It should be noted that cytochrome c has significantly less disorder associated with the heme than does deoxy Mb.[48] This probably accounts for the better agreement between theory and experiment in the cytochrome c system.

D. Alternative Models. An alternative possibility to account for the anomalous phase and amplitude behavior of the ν_{40} mode is a model recently proposed[51] in related studies of the ultrafast photodissociation of CO from cytochrome oxidase. This proposal suggests that sequential population transfer from the CO bound to the CO unbound state takes place as the heme oscillates (domes). The unusual phase and amplitude excitation profiles observed for the 47 cm^{-1} mode of cytochrome oxidase resemble the observations presented here for ν_{40} in Mb and are used by Liebl et al.[51] to rationalize the coherent population transfer model. However, we also see clear evidence for ν_{40} in deoxy Mb, where no reaction or population transfer event is taking place (see Fig. 1). Thus, it appears that ν_{40} represents a genuine vibrational coherence and the coherent population transfer model[51] can be eliminated from consideration (at least for Mb). The observation of ν_{40} in more sophisticated wavelength selective modulation experiments[46] on MbNO, which experimentally discriminate against population transfer signals, is also inconsistent with a coherent population transfer model for NO photodissociation.

Our assignment of ν_{40} and ν_{80} to heme doming[6,12,32] is in accord with the conclusions of Liebl et al.[51] However, we differ on the physical mechanism that generates the oscillatory signal. We suggest that the signal is a genuine vibrational coherence, triggered by the electron rearrangements associated with ligand photodissociation, and that a heterogeneous, anharmonic model, analogous to the one presented in the lower portion of Fig. 5, is the key to a quantitative understanding of the observations.

E. Collective Doming Motion. We note in closing that a mode analogous to ν_{40} has not yet been clearly observed[52] in recent high resolution synchrotron based experiments on Mb, which are sensitive to the vibrational spectrum of the ^{57}Fe at the active site. A suppression of the intensity of this mode in the detected Fe density-of-states would be explained if the iron motion represents a relatively small fraction of the total kinetic energy involved in the ν_{40} motion. This would be the case if there were significant collective motion that involved the surrounding protein or solvent material when the heme domes.[52]

This work was supported by grants from the National Institutes of Health DK35090 and the National Science Foundation MCB9904516.

References

1 N. F. Scherer, D. M. Jonas, G. R. Fleming, *J. Chem. Phys.*, **99**, 153 (1993).

2 N. Pugliano, A. Z. Szarka, R. M. Hochstrasser, *J. Chem. Phys.*, **104**, 5062 (1996).

3 M. Chachisvilis, H. Fidder, and V. Sundstrom, *Chem. Phys. Lett.*, **234**, 141 (1995).

4 J. C. Polanyi and A. H. Zewail, *Acc. Chem. Res.*, **28**, 119 (1995).

5 L. D. Ziegler, R. Fan, A. E. Desrosiers, and N. F. Scherer, *J. Chem. Phys.*, **100**, 1823 (1994).

6 L. Y. Zhu, J. T. Sage, and P. M. Champion, *Science*, **266**, 629 (1994).

7 M. H. Vos, F. Rappaport, J. C. Lambry, J. Breton, and J. L. Martin, *Nature*, **363**, 320 (1993).

8 S. Ruhman, A. G. Joly, and K. A. Nelson, *J. Chem. Phys.*, **86**, 6563 (1987).

9 A. H. Zewail, "Femtochemistry: Ultrafast Dynamics of the Chemical Bond," World Scientific Publishing Co. Pte. Ltd., Singapore, **1994**.

10 Q. Wang, R. W. Schoenlein, L. A. Peteanu, R. A. Mathies, and C. V. Shank, *Science* **266**, 422 (1994).

11 L. Y. Zhu, W. Wang, J. T. Sage, and P. M. Champion, *J. Raman Spectrosc.*, **26**, 527 (1995).

12 P. M. Champion, F. Rosca, W. Wang, A. T. N. Kumar, J. Christian, and A. Demidov, Proc. SPIE in "Laser Techniques for Condensed-Phase and Biological Systems," **3273**, 80 (1998).

13 S. M. Janes, G. A. Dalickas, W. A. Eaton, and R. M. Hochstrasser, *Biophys. J.*, **54**, 545 (1988).

14 A. Ansari, C. M. Jones, E. R. Henry, J. Hofrichter, and W. A. Eaton, *Biophys. J.*, **64**, 852 (1993).

15 T. A. Jackson, M. Lim, and P. A. Anfinrud, *Chem. Phys.*, **180**, 131 (1994).

16 S. Kaminaka, T. Ogura, and T. Kitagawa, *J. Am. Chem. Soc.*, **112**, 23 (1990).

17 D. G. Lambright, S. Balasubramanian, S. G. Boxer, *Chem. Phys.*, **158**, 249 (1991).

18 T. Nakabayashi, H. Okamoto, and M. Tasumi, *J. Phys. Chem. A*, **101**, 3494 (1997).

19 W. D. Tian, J. T. Sage, V. Srajer, and P. M. Champion, *Phys. Rev. Lett.*, **68**, 408 (1992).

20 V. Srajer, T. Y. Teng, T. Ursby, C. Pradervand, Z. Ren, S. Adachi, W. Schildkamp, D. Bourgeois, M. Wulff, and K. Moffat, *Science* **274**, 1726 (1996).

21 J. T. Sage, K. T. Schomacker, and P. M. Champion, *J. Phys. Chem.*, **99**, 3394 (1995).

22 K. N. Walda, X. Y. Liu, V. S. Sharma, and D. Magde, *Biochemistry*, **33**, 2198 (1994).

23 R. H. Austin, K. Beeson, L. Eisenstein, H. Frauenfelder, and I. C. Gunsalus, *Biochemistry*, **14**, 5355 (1975).

24 T. E. Carver, R. J. Rohlfs, J. S. Olson, Q. H. Gibson, R. S. Blackmore, B. A. Springer, and S. G. Sligar, *J. Biol. Chem.*, **265**, 20007 (1990).

25 V. Srajer, L. Reinisch, and P. M. Champion, *J. Am. Chem. Soc*., **110**, 6656 (1988).
26 V. Srajer and P. M. Champion, *Biochemistry* **30**, 7390 (1991).
27 P. M. Champion, *J. Raman Spectrosc*., **23**, 557 (1992).
28 M. F. Perutz, *Proc. R. Soc. Londser. B*, **208**, 135 (1980).
29 P. M. Kozlowski, T. G. Spiro, A. Berces, and M. Z. Zgierski, *J. Phys. Chem. B*, **102**, 2603 (1998).
30 T. G. Spiro, P. M. Kozlowski, and M. Z. Zgierski, *J. Raman Spectrosc*., **29**, 869 (1998).
31 P. M. Kozlowski, T. G. Spiro, and M. Z. Zgierski, *J. Phys. Chem. B*, **104**, 10659 (2000).
32 F. Rosca, A. T. N. Kumar, X. Ye, T. Sjodin, A. A. Demidov, and P. M. Champion, *J. Phys. Chem*., **104**, 4280 (2000).
33 W. Wang, A. A. Demidov, X. Ye, J. F. Christian, T. Sjodin, and P. M. Champion, *J. Raman Spectrosc*., **31**, 99 (2000).
34 F. Wise, M. Rosker, G. Millhauser, and C. L. Tang, *J. Quantum Electron*., **QE-23**, 1116 (1987).
35 A. T. N. Kumar, L. Zhu, J. F. Christian, A. A. Demidov, and P. M. Champion, *J. Phys. Chem*., **105**, 7847 (2001).
36 S. Constantine, Y. Zhou, J. Morais, and L. D. Ziegler, *J. Phys. Chem. A*, **101**, 5456 (1997).
37 P. M. Champion and R. Lange, *J. Chem. Phys*., **73**, 5947 (1980).
38 F. Adar, M. Gouterman, and S. Aronowitz, *J. Phys. Chem.* **80**, 2184 (1976).
39 P. M. Champion and G. J. Perreault, *J. Chem. Phys*., **75**, 490 (1981).
40 J. M. Friedman and D. L. Rousseau, *Chem. Phys. Lett*., **55**, 488 (1978).
41 R. M. Hochstrasser, "Probes of Structure and Function of Macromolecules and Membranes," Academic Press, New York, **1971**; p. 57.
42 A. A. Demidov, X. Ye, F. Rosca, A. T. N. Kumar, D. Ionascu, W. Wang, L. Zhu, and P. M. Champion, in preparation . **2001**. Ref. Type: in press.
43 A. T. N. Kumar, F. Rosca, A. Widom, and P. M. Champion, *J. Chem. Phys*., **114**, 701 (2001).
44 W. Wang, X. Ye, A. A. Demidov, F. Rosca, T. Sjodin, W. Cao, M. Sheeran, and P. M. Champion, *J. Phys. Chem. B*, **104**, 10789 (2000).
45 A. Desbois, M. Momenteau, B. Loock, and M. Lutz, *Spectrosc. Letters* **14**, 257 (1981).
46 F. Rosca, A. T. N. Kumar, D. Ionascu, T. Sjodin, A. A. Demidov, and P. M. Champion, *J. Chem. Phys*., **114**, 10884 (2001).
47 F. Rosca, D. Ionascu, A. T. N. Kumar, A. A. Demidov, and P. M. Champion, *Chem. Phys. Lett*., **337**, 107 (2001).
48 V. Srajer, K. T. Schomacker, and P. M. Champion, *Phys. Rev. Lett*., **57**, 1267 (1986).
49 A. T. N. Kumar, F. Rosca, A. Widom, P. M. Champion, *J. Chem. Phys*., **114**, 6795 (2001).
50 A. Tokmakoff and M. D. Fayer, *Acc. Chem. Res*., **28**, 437 (1995).
51 U. Liebl, G. Lipowski, M. Negrerie, J. C. Lambry, J. L. Martin, and M. H. Vos, *Nature*, **401**, 181 (1999).
52 J. T. Sage, S. M. Durbin, W. Sturhahn, D. C. Wharton, P. M. Champion, P. Hession, J. Sutter, and E. E. Alp, *Phys. Rev. Lett*., **86**, 4966 (2001).